IEEE Access
Multidisciplinary | Rapid Review | Open Access Journal

Received 22 May 2023, accepted 19 July 2023, date of publication 24 July 2023, date of current version 28 July 2023.

Digital Object Identifier 10.1109/ACCESS.2023.3298107

RESEARCH ARTICLE

Forward Scatter Shadow Ratio: Concept and Its Application in Shadow Profile Retrieval

XI SHEN, (Member, IEEE), AND DEFENG HUANG, (Senior Member, IEEE)
Department of Electrical, Electronic and Computer Engineering, The University of Western Australia, Perth, WA 6009, Australia
Corresponding author: Defeng Huang (david.huang@uwa.edu.au)

This work was supported in part by the Australian Research Council (ARC) under Grant DP220101894.

ABSTRACT Traditionally, the radar cross-section is used to characterize the target in a forward scatter radar (FSR) system, the measurement of which requires the availability of the scattered signal. However, the scattered signal is often hard to be extracted, particularly when the illumination signal is opportunistic. In this paper, we introduce the concept of the forward scatter shadow ratio (FSSR) of a target as the ratio of the total received power density to the incident power density for a receiver at a certain location in an FSR system. It is argued that the FSSR can be a useful parameter in the studies of FSR systems as it is relevant to target detection, size estimation, classification and shadow profile imaging. Particularly, using mathematical analysis and numerical results, we demonstrate that the shadow profile of a target can be retrieved with the FSSR. The three sources of error in shadow profile retrieval, i.e., uncentered line of observation, shadow profile discretization and approximation of the imaginary error function are discussed.

INDEX TERMS Forward scattering, radar cross section, shadow profile, diffraction.

I. INTRODUCTION

Forward scatter radar (FSR) refers to the special kind of bistatic radar where the transmitter, the target and the receiver are almost on a straight line. It has a rich history in application, dating back as early as 1930s, when French scientist Pierre David's system for aircraft detection was used in the French Air Force [1]. The early FSR systems were often called electromagnetic fence or barrier [2], as target detection was achieved by exploiting the target's Doppler signature when it crosses the transmitter-receiver baseline. In the past 30 years FSR has gained much attention in research because of its distinct advantage, i.e., the ability to detect stealth targets. Unlike monostatic radar, FSR is not based on the reflectivity of the target, thus it is suitable to detect targets with specific shapes and/or coatings that suppress backscattering. Moreover, the availability of illuminators of opportunity (IOs) has further boosted the research in this field. Passive FSR systems exploit existing transmitters and only require the design and implementation of the passive receiver, thus can potentially lead to a low-cost and low-complexity solution.

There are many studies reported in the literature investigating passive FSR systems with various IOs. For example, some studies have used signals of Global Navigation Satellite System (GNSS) for detection and classification of air targets [3], [4], [5], [6], marine targets [7] and ground targets [8]. It has also been reported that Digital Video Broadcasting (DVB) signals can also serve as good IOs [9], [10], [11]. Moreover, Wi-Fi signals [12], [13], [14] and Global System for Mobile Communications (GSM) signals [15] have been investigated as the signal source in passive FSR to detect and track ground-based targets, especially vehicles. FSR can also be used as Shadow Inverse Synthetic Aperture Radar (SISAR) for target imaging. Introduced by Chapurskiy in 1980s, the theory of SISAR indicates that the target's shadow profile can be extracted from the forward scatter signal in the Fresnel zone [16]. It has been reported that GNSS and DVB signals can be exploited as IOs for the purpose of SISAR imaging [17], [18], [19].

The rapid development in Low Earth Orbit (LEO) satellites has provided a new type of IOs for passive FSR applications. One example of such illuminator is the Starlink

The associate editor coordinating the review of this manuscript and approving it for publication was Davide Comite.

This work is licensed under a Creative Commons Attribution 4.0 License. For more information, see https://creativecommons.org/licenses/by/4.0/

constellation, which uses microwave signals for global Internet services [20]. The opportunistic use of signals form a network of a large number of LEO satellites can potentially serve monitoring purposes such as measuring rain and cloud [21], [22], [23]. It has been proposed that these signals can be used as IOs in an FSR setup for flying object detection [24] and for space debris tracking and imaging [24], [25], [26], [27], [28].

Existing studies of FSR mainly employ the concept of radar cross-section (RCS) from mono and traditional bistatic radar, which is named forward scatter cross-section (FSCS) [29], [30], to characterize the target. However, there are two problems associated with this paradigm. First, in FSR the received signal is always an outcome of interference between the forward scattering signal and the direct path signal (DPS), thereby the relationship between the FSCS and the received signal is not as straightforward as that for mono and bistatic radar. Secondly, in order to utilize the FSCS, one has to assume that the DPS can be removed. However, in reality for opportunistic use of passive IOs such as GNSS and the Starlink, traditional methods such as the square law detector cannot remove the DPS from the total received signal [31], [32].

In this paper, we introduce a new parameter to characterize the target specifically for FSR systems, namely the forward scatter shadow ratio (FSSR). The FSSR of a target is the ratio of the total received power density to the incident power density for a receiver at a certain location in an FSR system. It is a parameter to show specifically how far the total received signal deviates from the DPS, which the FSCS does not provide. The FSSR represents the target by using the total received signal without the need to extract the scattered field as the use of the FSCS. For instance, it can serve as a direct indicator for target detection in passive FSR systems. Furthermore, we will demonstrate that the FSSR is relevant to the target size estimation, classification and shadow profile imaging.

The Fresnel diffraction formula [33] is used in our analysis, with all distances and dimensions normalized with respect to the wavelength of the signal. Numerical results are used to demonstrate how the FSSR is affected by the normalized size and shape of the target, as well as the location of the receiver. When measured on a straight line on the observation plane that is perpendicular to the waveform propagation direction, the FSSR oscillates around 1 and has a maximum value and a minimum value. It is suggested that the maximum and minimum values of the FSSR are affected by the normalized distance between the target and the observation plane, as well as the size of the target. Using a circular target, we demonstrate that the minimum FSSR on the observation plane is a monotonically decreasing function of the normalized diameter, while the maximum FSSR is non-monotonic. When the observation plane is moved farther away from the target, both the minimum and the maximum FSSR will converge asymptotically to one.

Furthermore, we will show that the shadow profile of the target can be retrieved using discrete observations of the FSSR and a retrieval algorithm is then proposed. The target shadow profile is represented by a finite number of rectangular strips, the heights of which are retrieved using a number of discrete observations on a straight line. Retrieving strip heights is formulated as a nonlinear least-square problem, which is solved by a trust region method [34]. The retrieval method is dependent upon three approximations, namely, assuming that the observations are from a centered line, approximating the shadow profile by rectangular strips and employing the first term of the Maclaurin series to approximate the imaginary error function. The three approximations introduces three sources of errors. Firstly, as the line of FSSR observation is far away from the center, the error in the retrieved heights becomes more prominent. The distance of the line of observation from the center can provide a reference as to how large the error is. Secondly, numerical results suggest that choosing a lower resolution strips leads to a higher level of error. Thirdly, the far-field parameter, a parameter that is proportional the square of the target dimension divided by the distance between the target and the receiver, determines the level of error induced by the approximation of the imaginary error function. Numerical results confirm that the error can be reduced by including the cubic term of the Maclaurin series in the retrieval algorithm.

The proposed approach for target shadow profile retrieval differs from SISAR in mainly two aspects. Firstly, SISAR exploits the movement of the target with respect to the observation geometry and applies inverse Fresnel transform to the forward scatter signal. By comparison, the proposed method is an optimization method so it can accommodate discrete FSSR samples from different receiver locations. Secondly, SISAR estimates a continuous function of target height using the approximation of the Sinc function while the proposed method discretizes the target shadow profile into rectangular strips and then computes the height of each strip, which can use both the first and the cubic terms of the Maclaurin series.

Numerical results using a triangular target and a target of irregular shape suggest that the retrieved shadow profiles represented by a finite number of rectangular strips display agreement with the original target shapes. In practical applications of shadow profile retrieval, the FSSR needs to be estimated from the total received signal. It is suggested that the average of samples of the total received power can represent the power of the DPS. But for better estimations these samples need to be taken where the magnitude of oscillation in the total power is relatively small. Numerical results using the estimated FSSR from the total received power also suggest that the shadow profile can be retrieved for both the triangular target and the target of irregular shape.

The rest of this paper is organized as follows. The definition of the FSSR is in Section II. The proposed method of using the FSSR for target shadow profile retrieval is presented in Section III. Section IV discusses several issues that arise

from the approximation in the retrieval method. Numerical results in regard to the features of the FSSR, the target shadow profile retrieval and the sources of error in the retrieval process are given in Section V. Finally, Section VI concludes this paper.

II. DEFINITION OF FSSR

We define the FSSR (ε) of a target as the ratio of the total received power density (P_{tot}) to the incident power density (P_{inc}) for the receiver at a certain location, as follows:

$$\varepsilon = \frac{P_{tot}}{P_{inc}} = \frac{|E_{tot}|^2}{|E_{inc}|^2}. \tag{1}$$

In (1), E_{tot} and E_{inc} are the complex amplitudes of the total electric field and the incident electric field, respectively. Note that the total electric field is the outcome of the interference between the incident electric field and the forward scatter field caused by the target. An illustration of the FSSR can be found in Fig. 1. Similar to the FSCS (and to RCS), the FSSR also utilize a ratio of power density. However, the FSCS is a description of the target based on the forward scatter field regardless of the range of the observation point. It is a function of the azimuth and elevation angles and it is in the unit of area. On the other hand, the FSSR uses the total electric field rather than the forward scatter radiation. It is a dimensionless parameter and dependent on the location of the observation point. The FSSR observed on two planes with different distances from the target is shown in Fig. 1.

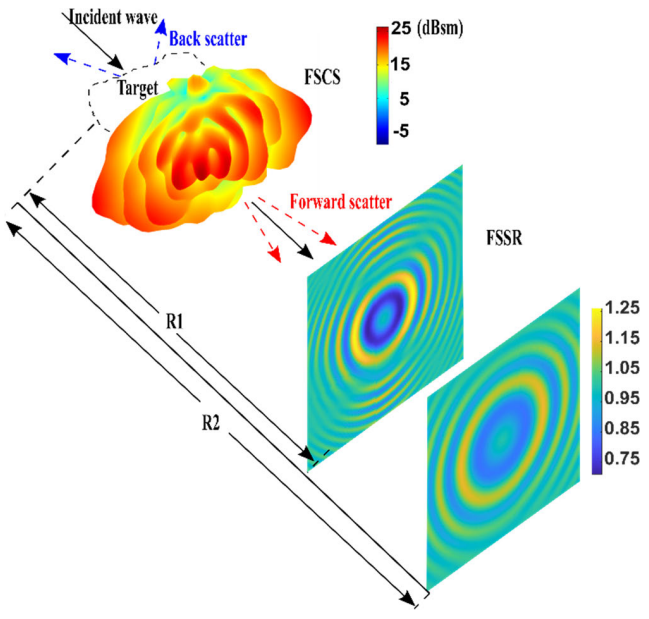

FIGURE 1. An illustration of FSCS and FSSR in an FSR system.

Note that similarly the total received signals have been used in the literature [35], [36], [37] to obtain the time-domain signature,[1] but not explicitly used in a parameter to describe the target in the FSR systems, However, besides FSCS, no new target parameter has been defined in [35], [36], and [37]. The time-domain signature is dependent on the movement of the target with respect to the FS geometry. In the case where there is no or very little target movement, the time-domain signature cannot be used as it is totally removed by the DC remover.

Without loss of generality, consider a plane wave propagating in the y direction of a Cartesian system, illuminating a target (Fig. 2). The geometric center of the target is located at the origin. The receiver is located on an observation plane perpendicular to the -axis and its projection on the y axis is R from the origin. Using Babinet's principle and the Fresnel diffraction formula, we can replace the target with a complementary aperture that has the shape of the target shadow silhouette on the $x'-z'$ plane and obtain the complex amplitude of the diffraction field E_D [33]:

$$E_D(x, z, R) = \frac{e^{2\pi Ri}}{iR} \iint F(x', z')\, e^{\frac{\pi i}{R}[(x-x')^2+(z-z')^2]} dx' dz' \tag{2}$$

where the imaginary unit is denoted by i, and R, x, z, x' and z' are all normalized with respect to the wavelength of the signal, so they are dimensionless. For instance, R denotes how many wavelengths there are from the origin to the observation plane. Some examples of the normalized value for different wavelengths can be found in Table 1. The aperture function $F(x', z')$ is given by

$$F(x', z') = \begin{cases} 1, & \{x', z'\} \in \Sigma \\ 0, & \text{otherwise} \end{cases} \tag{3}$$

where Σ is the target shadow silhouette on the $x' - z'$ plane.

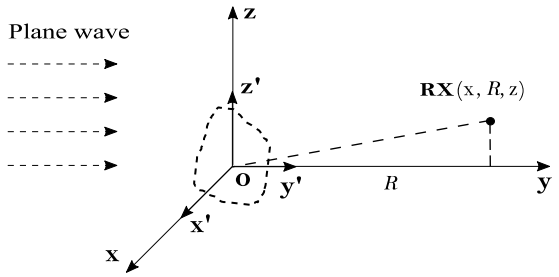

FIGURE 2. An illustration of an idealized forward scatter radar system.

It is worth noting that the Fresnel diffraction formula is an approximation of the Rayleigh-Sommerfeld diffraction formula when the range of observation is large comparing to the target size. The Fresnel diffraction formula has been used extensively in the studies of FSR systems [16], [28]. On the

[1]The extraction of the time-domain signature involves a self-mixing heterodyne [9], [32], a low-pass filter and a remover for the DC component [37] Essentially, it is a function of the DPS, the FSCS, the motion parameters and the distance between the transmitter and the receiver.

TABLE 1. Normalized values of distances and dimensions.

Normalized Value: R/x′ / λ	R		x′	
	1 km	10 km	0.2 m	1 m
λ = 1 cm	1×10^5	1×10^6	20	100
λ = 5 cm	2×10^4	2×10^5	4	20

other hand, the Helmholtz-Kirchhoff formula, which is equivalent to the Rayleigh-Sommerfeld formula at moderate angles of diffraction when the wavelength is small with respect to the target size [38], has also been widely used [36], [39]. Generally, the Fresnel formula has a simpler form than the Helmholtz-Kirchhoff formula, and the approximation only induces marginal errors in the FSR setup.

The complex amplitude of the total electric field is

$$E_{tot} = E_{inc} - E_D = e^{2\pi Ri} - E_D. \tag{4}$$

In (4), the incident field E_{inc} denotes the DPS, which is the signal when the target is assumed absent. The FSSR is the ratio of the power density of the total signal due to the presence of the target to that of the DPS. Intuitively, the FSSR deviating from one indicates that there is forward scattering from an object interfering with the DPS. From (1) to (4), we rewrite ε as

$$\varepsilon = \left| 1 - \frac{1}{iR} \iint F\left(x', z'\right) e^{\frac{\pi i}{R}\left[(x-x')^2 + (z-z')^2\right]} dx' dz' \right|^2. \tag{5}$$

III. TARGET SHADOW PROFILE RETRIEVAL WITH FSSR

From (5), we define

$$A_F(x, z) = \iint F\left(x', z'\right) e^{\frac{\pi i}{R}\left[(x-x')^2 + (z-z')^2\right]} dx' dz', \tag{6}$$

which is the Fresnel integral for the aperture $F\left(x', z'\right)$. To further simplify the equation we assume a centered line of FSSR observation,[2] i.e., the FSSR is observed on a line that passes through the projection of the geometric center of the target on the observation plane. Then the centered line of observation is defined as $x = 0$ on the observation plane, and the integration consequently becomes

$$A_F(z) = \int \int F\left(x', z'\right) e^{\frac{\pi i}{R}x'^2} e^{\frac{\pi i}{R}(z-z')^2} dx' dz' \tag{7}$$

We divide the target shadow into N strips with equal width and each individual strip p is regarded as a rectangle (Fig. 3 for illustration). The integration in (7) can be approximated as

$$A_F(z) \approx \sum_{p=1}^{N} \int_{b_p}^{a_p} e^{\frac{\pi i}{R}x'^2} dx' \int_{d_p}^{c_p} e^{\frac{\pi i}{R}(z-z')^2} dz' \tag{8}$$

where a_p and b_p respectively mark the x' coordinates of the top and bottom sides of the strip p, while c_p and d_p respectively mark the z' coordinates of its right and left sides.[3] The first integration in (8) is given by

$$\int_{b_p}^{a_p} e^{\frac{\pi i}{R}x'^2} dx' = \frac{1}{2}\sqrt{\frac{R}{i}}\left(erfi\left(\sqrt{\frac{i\pi}{R}} a_p\right) - erfi\left(\sqrt{\frac{i\pi}{R}} b_p\right)\right) \tag{9}$$

where $erfi(x)$ is the imaginary error function, whose Maclaurin series is [40]

$$erfi(x) = \frac{2}{\sqrt{\pi}}\left(x + \frac{x^3}{3} + \frac{x^5}{10} + \cdots + \frac{x^{2n+1}}{n!\,(2n+1)}\right). \tag{10}$$

This indicates that if the conditions $\left|\sqrt{\frac{i\pi}{R}} a_p\right| \ll 1$ and $\left|\sqrt{\frac{i\pi}{R}} b_p\right| \ll 1$ can be satisfied, we have

$$\int_{b_p}^{a_p} e^{\frac{\pi i}{R}x'^2} dx' \approx a_p - b_p = h_p, \tag{11}$$

where h_p is the height of the strip p. As a result,

$$A_F(z) = \sum_{p=1}^{N} h_p \int_{d_p}^{c_p} e^{\frac{\pi i}{R}(z-z')^2} dz'. \tag{12}$$

We define $G_p(z)$

$$G_p(z) = \int_{d_p}^{c_p} e^{\frac{\pi i}{R}(z'-z)^2} dz' = \sqrt{\frac{R}{4i}}\left(erfi\left(\sqrt{\frac{i\pi}{R}}(c_p - z)\right) - erfi\left(\sqrt{\frac{i\pi}{R}}(d_p - z)\right)\right) \tag{13}$$

then

$$\varepsilon(z) = \left| 1 - \frac{1}{iR} \sum_{p=1}^{N} h_p G_p(z) \right|^2. \tag{14}$$

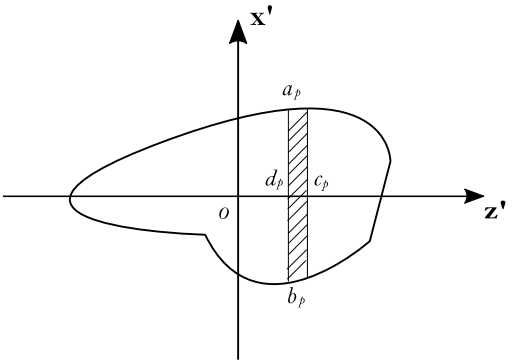

FIGURE 3. The target shadow is divided into strips, one of which is shown by the shaded area. Each strip is regarded as a rectangle.

[2]The line of FSSR observation can be formed either by a fixed target and a moving receiver or by a fixed receiver and a moving target.

[3]If the target shadow is in a concave shape, some of the strips may have holes in the middle, in which case the first integration in (8) will be the sum of several separate integrations.

Suppose that there are M observations $\varepsilon_q(z_q)$ at $(0, R, z_q)$, $q = 1, \cdots, M$, solving h_p can be formulated as a nonlinear least-square problem:

$$\hat{h} = \arg\min S(\mathbf{h}), \tag{15}$$

in which $\mathbf{h}$ is the vector representation of h_p and

$$S(\mathbf{h}) = \sum_{q=1}^{M} r_q^2, \tag{16}$$

with

$$r_q = \varepsilon_q(z_q) - \left| 1 - \frac{1}{iR} \sum_{p=1}^{N} h_p G_p(z_q) \right|^2. \tag{17}$$

By minimizing $S(\mathbf{h})$, the optimal values for h_p can be found and thus the shadow profile of the target is retrieved.[4] There are several algorithms readily available to numerically solve the nonlinear least-square problem. The most used one is the trust region method [34], which has been proven to generate strictly feasible iterates and offer strong convergence properties. In this paper, we propose to use the default trust-region-reflective algorithm available in MATLAB, which possesses the ability to deal with complex-valued problems.

IV. DISCUSSION ON RESOLUTION OF THE RETRIEVAL METHOD

In the retrieval method described above, given R, $G_p(z)$ is known only if the location and width of the strips are given. In order to solve strip heights h_p, the width of the strips, i.e., the desired resolution of the retrieval, must be assumed first. Furthermore, (13) indicates that given $G_0(z)$, the value of $G_p(z)$ is merely the horizontal translations of $G_0(z)$. Consider $G_0(z)$ given by

$$G_0(z) = \int_{d_0}^{c_0} e^{\frac{\pi i}{R}(z'-z)^2} dz', \tag{18}$$

As an example for $c_0 = 10$, $d_0 = -10$ and $R = 10^5$, the real and imaginary parts of $G_0(z)$ are plotted in Fig. 4. When R is increased to 10^6 (c_0 and d_0 not changed), the real and imaginary parts of $G_0(z)$ are plotted in Fig. 5(a) and 5(b), respectively. Then we change c_0 and d_0 to $c_0 = 50$ and $d_0 = -50$, the real and imaginary parts of $G_0(z)$ are plotted in Fig. 5(c) and 5(d), respectively. It is worth noting that the function to be integrated in (18) for $z = 0$ is exactly the same as that in (11). Hence, we can justify the approximation in (11) by examining the real and imaginary values of $G_0(0)$. For instance, the real part for $z = 0$ in Fig. 4(a) is approximately 20 (which is the value of $c_0 - d_0$ according to (11)), and the imaginary part is very close to zero (0.02094 in Fig. 4(b)). It can be concluded from Figs. 4 and 5 that the approximation of (11) is accurate when

[4]Compared to SISAR, which uses inverse Fresnel transformation, the proposed approach for shadow profile retrieval is an optimization method, and is able to accommodate discrete observations from different receiver locations.

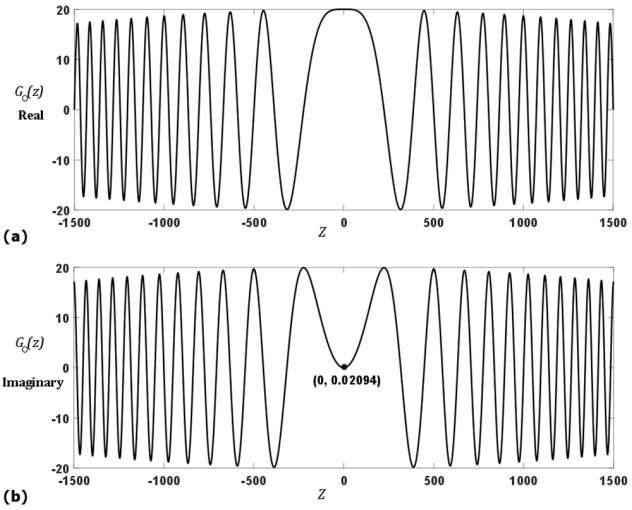

FIGURE 4. The real (a) and imaginary (b) values of $G_0(z)$ for (18), for $R = 10^5$, $c_0 = 10$ and $d_0 = -10$.

a_p and b_p are small compared with R. From (6) to (11), we can see that there are three approximations in the shadow profile retrieval algorithm. Each approximation will introduce some error which affects the accuracy of the retrieval. The first approximation is to assume that the FSSR is observed on the line of $x = 0$ on the observation plane. The second approximation is the target shadow profile discretization, i.e., dividing the shadow shape into multiple rectangular strips. In general, less number of strips will induce a higher level of error, but the error will depend on the shape of the target, which will be discussed using numerical results in the next section. The third is the approximation in (11) under the condition that $\left|\sqrt{\frac{i\pi}{R}} a_p\right| \ll 1$ and $\left|\sqrt{\frac{i\pi}{R}} b_p\right| \ll 1$. Because a_p and b_p can represent the physical dimensions of the target, the condition above can be approximately regarded as the far-field condition defined by the far-field parameter S [32]:

$$S = \frac{2h^2}{R} \ll 1, \tag{19}$$

in which h is the largest dimension (normalized with respect to the wavelength) of the target. In this section, we will conduct our analysis for both far-field scenarios and close to near-field scenarios where $S \approx 1$.

A. POSITION OF LINE OF OBSERVATION AND SHADOW PROFILE DISCRETIZATION

In the first approximation, the centered line of FSSR observation ($x = 0$) is a prerequisite in the retrieval method, so the first integration in (8) can then be associated with strip heights, given by (11). When $x \neq 0$, this approximation will result in errors in the retrieved heights. To investigate the impact of $x \neq 0$, consider a strip of height h_p and width $2c$ shown in

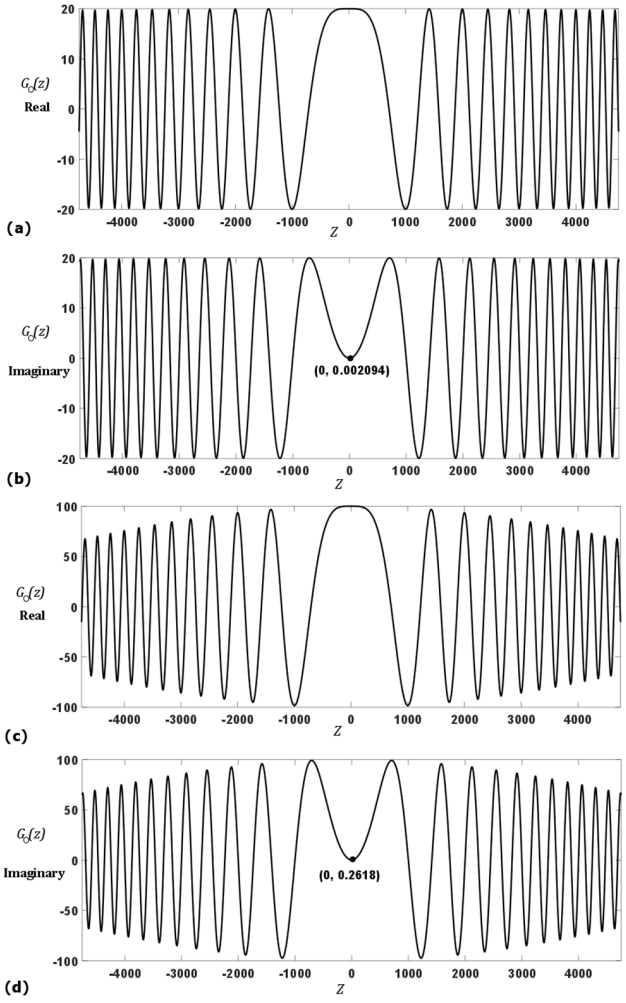

FIGURE 5. The real (a) and imaginary (b) values of $G_0(z)$, for $R = 10^6$, $c_0 = 10$ and $d_0 = -10$. The real (c) and imaginary (d) values of $G_0(z)$, for $R = 10^6$, $c_0 = 50$ and $d_0 = -50$.

Fig. 6(a), we define

$$B(z) = \int_{-\frac{h_p}{2}}^{\frac{h_p}{2}} e^{\frac{\pi i}{R}(x-x')^2} dx' \int_{-c}^{c} e^{\frac{\pi i}{R}(z-z')^2} dz', \tag{20}$$

where

$$\int_{-\frac{h_p}{2}}^{\frac{h_p}{2}} e^{\frac{\pi i}{R}(x-x')^2} dx' = \sqrt{\frac{R}{4i}} \left(\text{erfi}\left(\sqrt{\frac{i\pi}{R}} \left(\frac{h_p}{2} - x \right) \right) - \text{erfi}\left(\sqrt{\frac{i\pi}{R}} \left(-\frac{h_p}{2} - x \right) \right) \right) \tag{21}$$

According to (10), if the following can be satisfied

$$\begin{cases} \sqrt{\frac{1}{R}} \left| \frac{h_p}{2} - x \right| \ll 1 \\ \sqrt{\frac{1}{R}} \left| -\frac{h_p}{2} - x \right| \ll 1, \end{cases} \tag{22}$$

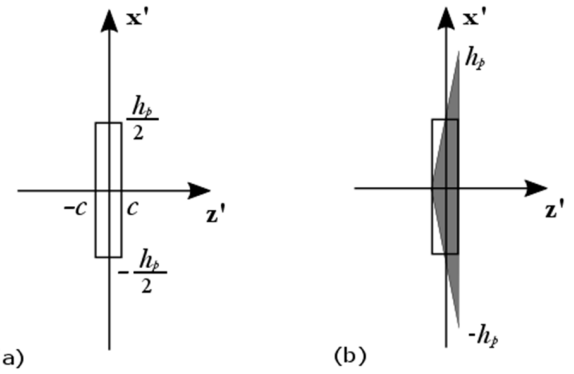

FIGURE 6. (a) An example strip and its dimensions. (b) The triangle (grey) that has the same width and the same area as the example strip (solid line).

then (21) can be reduced to h_p.We define

$$F(z) = h_p \int_{-c}^{c} e^{\frac{\pi i}{R}(z-z')^2} dz', \tag{23}$$

and

$$C(z) = B(z) - F(z). \tag{24}$$

We use $C(z)$ to represent the difference between the true value $B(z)$ and the approximation $F(z)$. As the first example, we consider a far-field scenario where $h_p = 100$ and $R = 10^5$. The plots of $B(z)$, $F(z)$ and $C(z)$ for $c = 10$ are given in Fig. 7. When x is fixed at 80 and 160, the real and imaginary parts of $B(z)$ are respectively shown in Fig. 7(a) and Fig. 7(b) and compared with $F(z)$. It is confirmed that $F(z)$ is close to $B(z)$, particularly for $x = 80$. As x becomes larger, $B(z)$ deviates further from $F(z)$, which indicates that the error induced by assuming $x = 0$ becomes larger. The plot of $C(z)$ for $x = 80$ is shown in Fig. 7(c). It is suggested that both the real and imaginary parts of $C(z)$ oscillate around 0 and they have nearly identical maximum and minimum values. When z takes a larger range, the real part of $C(z)$ is plotted in Fig. 7(d). It is suggested that the maximum and minimum values of $C(z)$ occurs near $z = 0$.

The range of $C(z)$ is a good indicator of the approximation error due to $x \neq 0$, thus we define

$$C_{max} = |C(z)|, \tag{25}$$

and plot C_{max} against x (shown by the solid line in Fig. 8).

Intuitively, as x increases, at a certain point the error becomes so large that the retreival result is not valid anymore. Here we employ an extreme case of shape approximation, which can provide a reference for the error. Consider a triangle that has the same width and the same area as the unit strip, shown by the grey triangle in Fig. 6(b). Let

$$J(z) = \int_T \int e^{\frac{\pi i}{R}x'^2} e^{\frac{\pi i}{R}(z-z')^2} dx' dz' \tag{26}$$

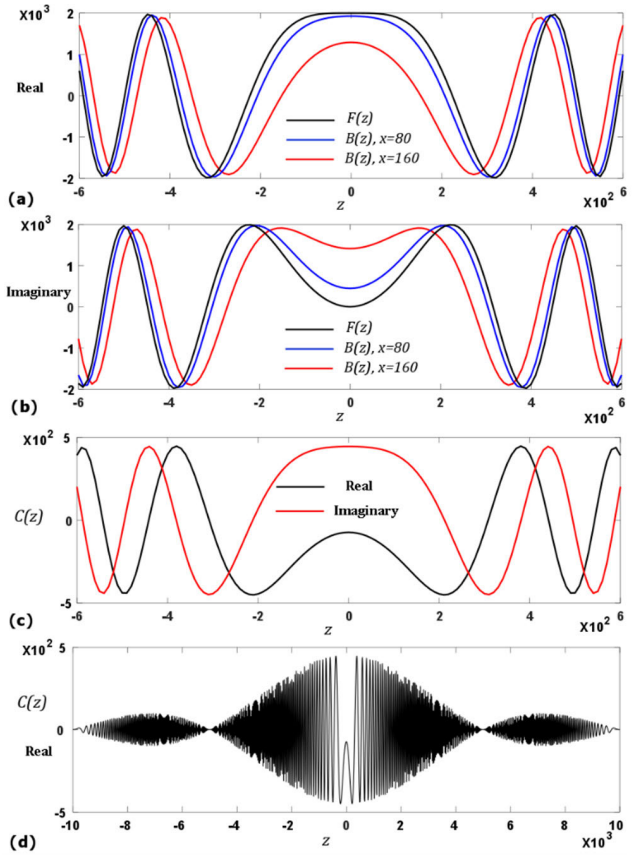

FIGURE 7. (a) The real part of function $B(z)$ when x is 80 (blue) and 160 (red), compared with function $F(z)$ (black). (b) The imaginary part of function $B(z)$ when x is 80 (blue) and 160 (red), compared with function $F(z)$(black). (c) The real (black) and imaginary (red) parts of function $C(z)$ for $-600 \le z \le 600$. (d) The real part of function $C(z)$ for $-10^4 \le z \le 10^4$.

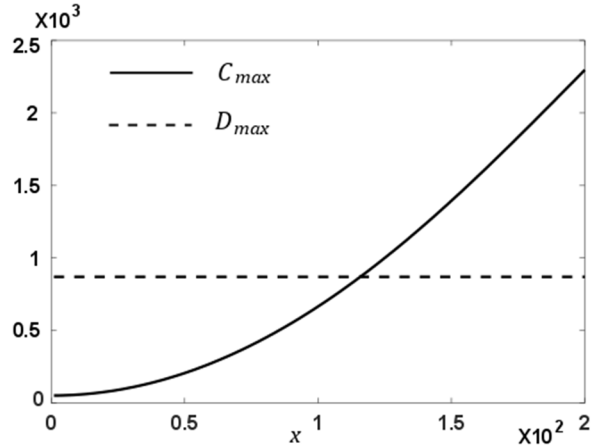

FIGURE 8. C_{max} as x increases (solid line) and the value of D_{max} (dashed line).

in which the double integral is performed over the triangle T, and

$$D(z) = J(z) - F(z). \tag{27}$$

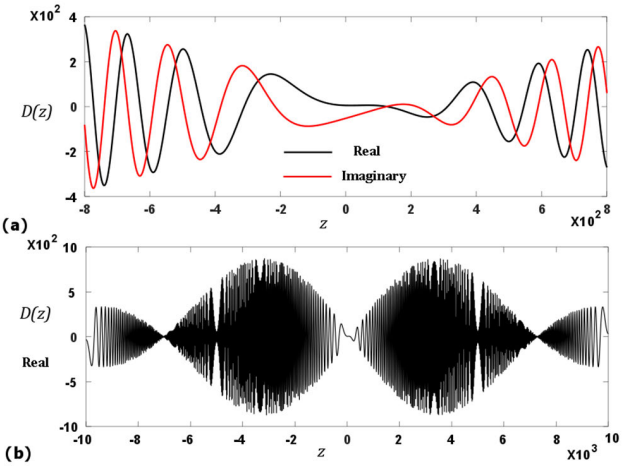

FIGURE 9. (a) The real (black) and imaginary (red) parts of function $D(z)$ for $-800 \le z \le 800$. (b) The real part of function $D(z)$ for $-10^4 \le z \le 10^4$.

In this extreme case the triangle is approximated by the rectangular strip (shown in Fig. 6(b)), and the approximation yields a big error due to the difference between the two shapes. The error is represented by $D(z)$, the real and imaginary parts of which around $z = 0$ are shown in Fig. 9(a). It can be seen that they also oscillate around zero, and that they reach similar maximum and minimum values. We define

$$D_{max} = |D(z)|, \tag{28}$$

the plot of the real part of $D(z)$ for a larger range (Fig. 9(b)) reveals that different from C_{max}, D_{max} occurs some distance from $z = 0$.

The value of D_{max} is calculated and marked by the dashed line in Fig. 8, which intersects with the curve for C_{max} at approximately $x = 120$. This indicates that for $h_p = 100$ and $c = 10$, the error caused by the approximation in (11) exceeds the error caused by approximating a triangle with a rectangular strip, when x exceeds approximately 120. In other words, for $x > 120$ it will be nonsensical to use finer strips (a resolution less than 20 for the example case) to approximate the shape because the error due to the nonzero x is even larger than the error caused by using the current strips. Fig. 8 implies that the resolution of 20 is achievable only if x is less than 120. The analysis above can be applied to a strip with any width and height so that the value of x can be related to the desired resolution of the shadow profile retrieval.

In Fig. 10, the results for the same far-field condition while c is increased to 25 (i.e., a resolution of 50) are shown. The real and imaginary parts of $B(z)$ compared with $F(z)$ are shown in Fig. 10(a) and Fig. 10(b), respectively. The plot of $C(z)$ for $x = 80$ is shown in Fig. 10(c), while the real part of $C(z)$ for a longer range is in Fig. 10(d). The real and imaginary parts of $D(z)$ are shown in Fig. 10(e) and the real part of $D(z)$ for a larger range is in Fig. 10(f). The values of D_{max} (dashed line) and C_{max} (solid line) are plotted in Fig. 10(g). For this strip with a larger width, the analysis

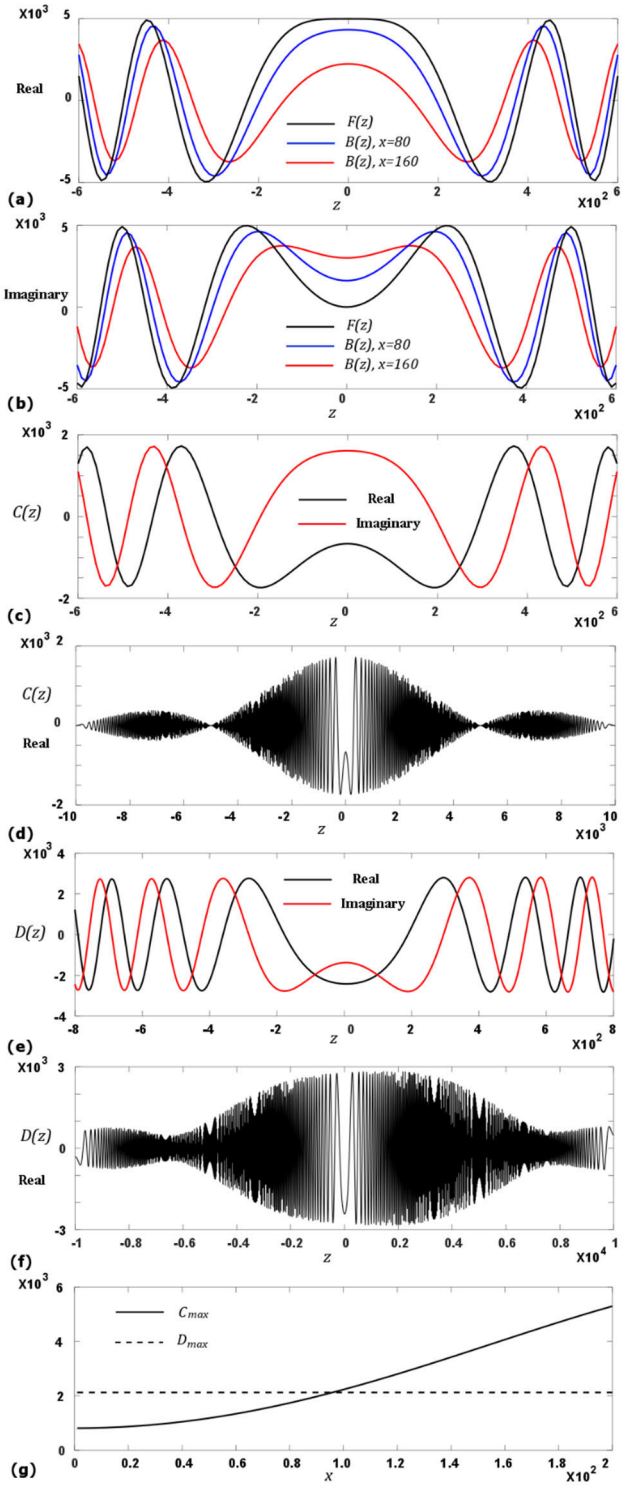

FIGURE 10. For $h_p = 100$ and $c = 25$. (a) The real part of function $B(z)$ when x is 80 (blue) and 160 (red), compared with function $F(z)$ (black). (b) The imaginary part of function $B(z)$, also compared with function $F(z)$(black). (c) The real (black) and imaginary (red) parts of function $C(z)$ for $-600 \le z \le 600$. (d) The real part of function $C(z)$ for $-10^4 \le z \le 10^4$. (e) The real (black) and imaginary (red) parts of function $D(z)$) for $-800 \le z \le 800$. (f) The real part of function $D(z)$ for $-10^4 \le z \le 10^4$. (g) C_{max} (solid line) as x increases and the value of D_{max} (dashed line).

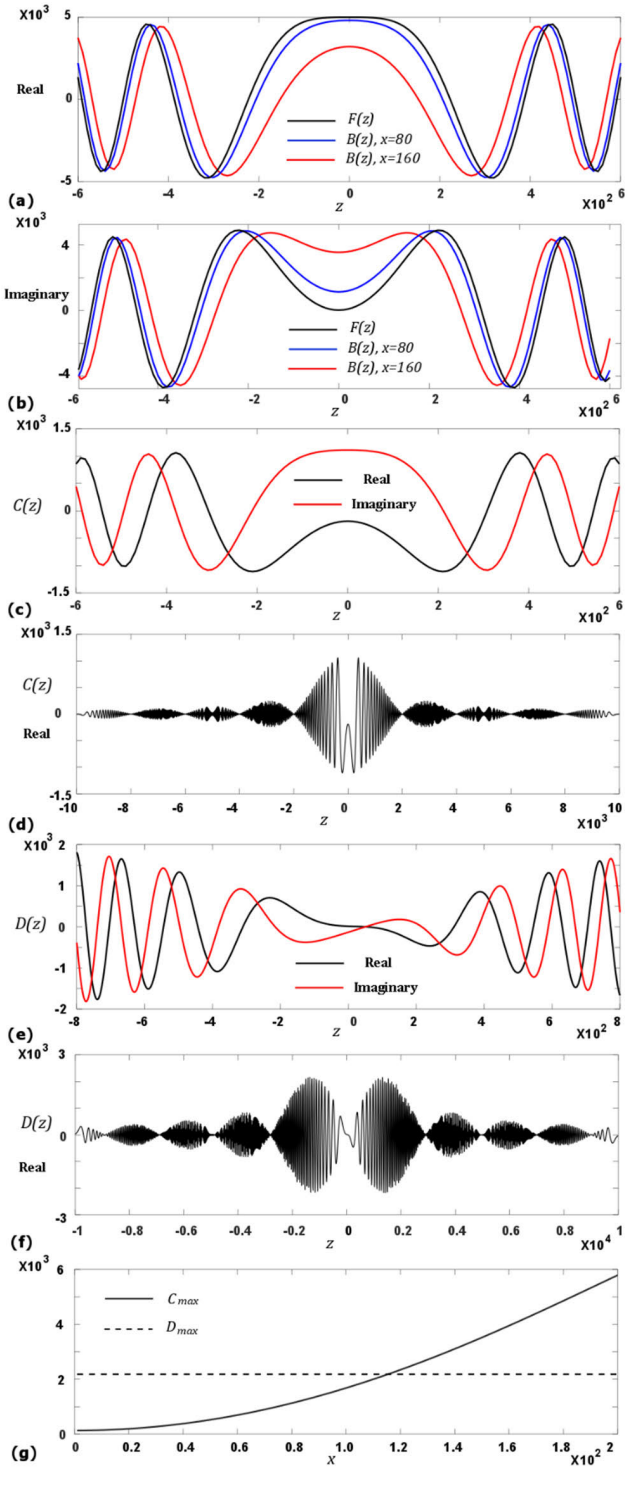

FIGURE 11. For $h_p = 250$ and $c = 10$. (a) The real part of function $B(z)$ when x is 80 (blue) and 160 (red), compared with function $F(z)$ (black). (b) The imaginary part of function $B(z)$, also compared with function $F(z)$(black). (c) The real (black) and imaginary (red) parts of function $C(z)$ for $-600 \le z \le 600$. (d) The real part of function $C(z)$ for $-10^4 \le z \le 10^4$. (e) The real (black) and imaginary (red) parts of function $D(z)$ for $-800 \le z \le 800$. (f) The real part of function $D(z)$ for $-10^4 \le z \le 10^4$. (g) C_{max} (solid line) as x increases and the value of D_{max} (dashed line).

suggests that the resolution of 50 is only achievable if x is less than 100, which is similar to that for $c = 10$.

Then we consider a close to near-field scenario where the strip height is 250 (far-field parameter S is 1.25, c is 10). The analytical results are shown in Fig. 11 in the same order as those in Fig. 10, which indicate that the resolution of 20 is only achievable if x is less than 120. Transitioning to near-filed does not have a significant effect on the restriction on line of observation position.

B. LINEAR APPROXIMATION

For the approximation by (11), we only use the first term of the Maclaurin series, under the condition that $\left|\sqrt{\frac{i\pi}{R}}a_p\right| \ll 1$ and $\left|\sqrt{\frac{i\pi}{R}}b_p\right| \ll 1$. We define

$$\begin{cases} a_p = \frac{1}{2}h_p + x_0 \\ b_p = -\frac{1}{2}h_p + x_0, \end{cases} \tag{29}$$

where x_0 is the x-coordinate of the center of the strip. We also define the approximated function $\hat{F}(x_0, h_p)$ and rewrite (11) as:

$$\hat{F}\left(x_0, h_p\right) = \int_{b_p}^{a_p} e^{\frac{\pi i}{R}x'^2} dx' \approx h_p, \tag{30}$$

taking into account the cubic term in (10), we can obtain

$$\hat{F}\left(x_0, h_p\right) \approx h_p + \frac{\pi i}{3R}\left[h_p^3 + 3h_p\left(x_0^2 - \frac{1}{4}h_p^2\right)\right]. \tag{31}$$

If $x_0 \ll h_p$, (31) can be simplified to

$$\hat{F}\left(h_p\right) \approx h_p(1 + \frac{\pi i}{12R}h_p^2). \tag{32}$$

Similarly, taking into account the quintic term in (10) and applying $x_0 \ll h_p$, we can obtain

$$\hat{F}\left(h_p\right) \approx h_p(1 + \frac{\pi i}{12R}h_p^2 - \frac{\pi^2}{160R^2}h_p^4). \tag{33}$$

The analysis above indicates that the cubic and quintic terms of the approximation are only a function of the far-field parameter S if the strip is close to the center of the target. Equations (32) and (33) also suggest that S determines the benefits of including the cubic term. As the far-field parameter becomes larger (i.e., transitioning to near-field), it is necessary to take into account the cubic, or even the quintic term of the Maclaurin series of the erfi function. In Fig. 12, we plot the true values (real and imaginary, shown by the black lines) of the integration of (30) for $x_0 = 0$ while h_p increases from 200 to 500 for both $R = 10^5$ and $R = 2 \times 10^5$, and compare them with the approximation given by (30), (32) and (33). The approximation in (30) has a real part h_p (shown by the blue line in Fig. 11(a)), and is imaginary part is zero (shown by the blue line in Fig. 11(b)). Equation (32) has an updated imaginary part (red lines in Fig. 11(b)), and (33) has an updated real part (red lines in Fig. 11(a)). The close to near-field case is represented by $R = 10^5$, for which the approximation in (30) and (32) yields more significant errors as S becomes larger. For $R = 2 \times 10^5$, the far-field parameter is less and the errors induced by (32) and (33) are almost invisible, which also justifies that the error level is determined by S. It is obvious that the computational load will be higher if we use (32) or (33) instead of (30) in the nonlinear least-squares algorithm. Nonetheless, it is suggested in the next section that h_p is still numerically solvable with the trust region method.

In conclusion of Sections IV-A and IV-B, the far-field parameter has a significant influence on the accuracy of the linear approximation, but has an insignificant effect on the restriction on the location of the observation line. A summary of the numerical results in this section and their corresponding far-field parameters can be found in Table 2.

TABLE 2. Numerical results and their far-field parameters.

Far-field	Figs. 7-9, $S = 0.2$
	Fig. 10, $S = 0.2$
	Fig. 12, $0.4 \le S \le 0.8$ ($R = 2 \times 10^5$, $200 \le h_p \le 200\sqrt{2}$)
Close to Near-Field	Fig. 11, $S = 1.25$
	Fig. 12, $0.8 \le S \le 5$ ($R = 10^5$, $200 \le h_p \le 500$)
	Fig. 12, $0.8 \le S \le 2.5$ ($R = 2 \times 10^5$, $200\sqrt{2} \le h_p \le 500$)

V. NUMERICAL RESULTS

A. FSSR OF CIRCLE, SQUARE AND EQUILATERAL TRIANGLE

We use the forward scatter radar model illustrated in Fig. 2 for the numerical analysis. Three different target shadow shapes, a circle, a square and an equilateral triangle, are considered and (5) is used to generate the FSSR. Figure 13 shows the FSSR for the three shadow shapes each with an area of 10^4 when the observation plane is located 10^5 from the origin ($R = 10^5$). The FSSR is only observed on the line of $x = 0$ on the observation plane. The maximum and minimum values of the FSSR, which occur very close to the -axis, are predominantly related to the shadow area of the target, but not significantly affected by the shadow shape. On the other hand, the change patterns of the FSSR display different characteristics for the three shadow shapes. It can be observed in Fig. 13 that the number of peaks when z is between 0 and 20 is different for the three shapes. Furthermore, the envelope of the oscillating pattern of the FSSR also displays distinct features for each shape. The change patterns of the FSSR may be used for target classification.

We use a circle of diameter D to further investigate the minimum and maximum values of the FSSR on the line of $x = 0$. In Fig. 14(a), it is shown how $\varepsilon_{\min}$ and $\varepsilon_{\max}$ change when D is from 10 to 500 ($R = 10^5$). It is suggested that when the size of the circle increases, $\varepsilon_{\min}$ monotonically decreases but $\varepsilon_{\max}$ can either increase or decrease. In Fig. 14(b), $\varepsilon_{\min}$ and $\varepsilon_{\max}$ are recorded for distance R ranging from 10^5 to 10^7 ($D = 100$). Both $\varepsilon_{\min}$ and $\varepsilon_{\max}$ approach 1 as the observation

plane moves further from the target. It can be concluded that the maximum and minimum values of the FSSR are affected by the normalized distance between the target and the receiver, as well as the size of the target.

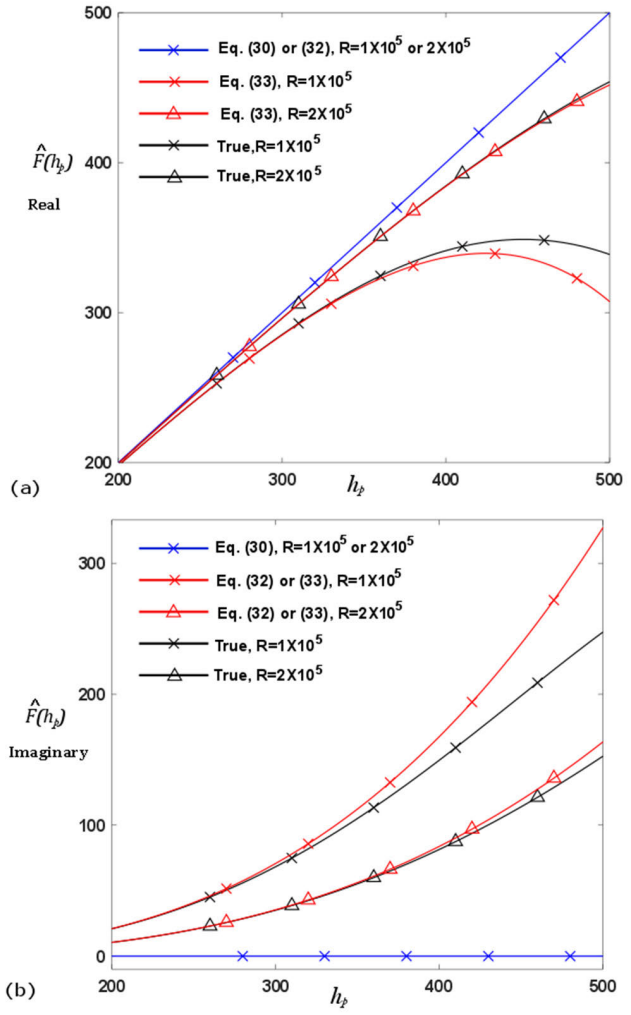

FIGURE 12. The real (a) and imaginary (b) parts of the true value of the intergration (black), and approximated values of using (30), (32) and (33) (colored lines).

The value of the FSSR deviating from 1 can be an effective indicator for target detection. For system design in practical applications the deviation needs to exceed a certain threshold for target detection. Particularly, $\varepsilon_{\min}$ may be used to determine if a target is detected. We plot D against R for $\varepsilon_{\min} = 0.8$ (dashed line) and $\varepsilon_{\min} = 0.9$ (solid line) in Fig. 15. This plot shows the minimum diameter for $\varepsilon_{\min}$ to fall below 0.9 and 0.8. For example, when $R = 10^6$, a circle of diameter more than 390 will have result in $\varepsilon_{\min}$ below 0.8. This feature of the FSSR may be used to design the threshold for target detection.

B. RETRIEVAL OF TARGET SHADOW PROFILE

We assume that the FSSR is available without any errors for target profile retrieval. Estimation of the FSSR through measurements of P_{tot} will be discussed in Section V-D. Since

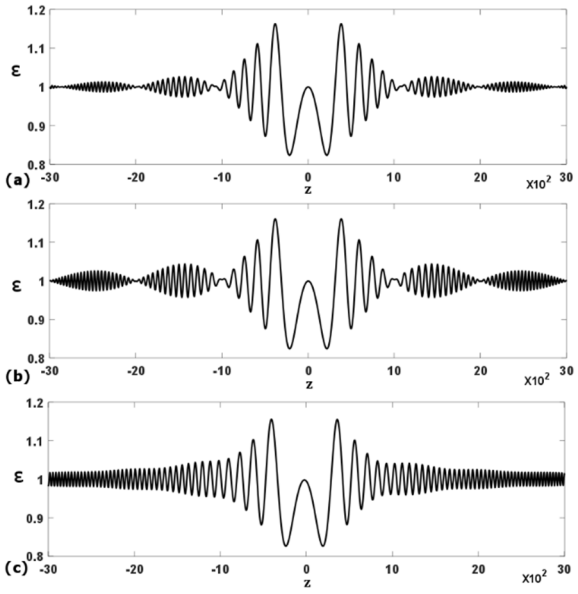

FIGURE 13. The FSSR on an observation plane of distance 10^5 from the target for three different shadow shapes. (a) A circle with an area of 10^4. (b) A square with an area of 10^4. (c) An equilateral triangle with an area of 10^4.

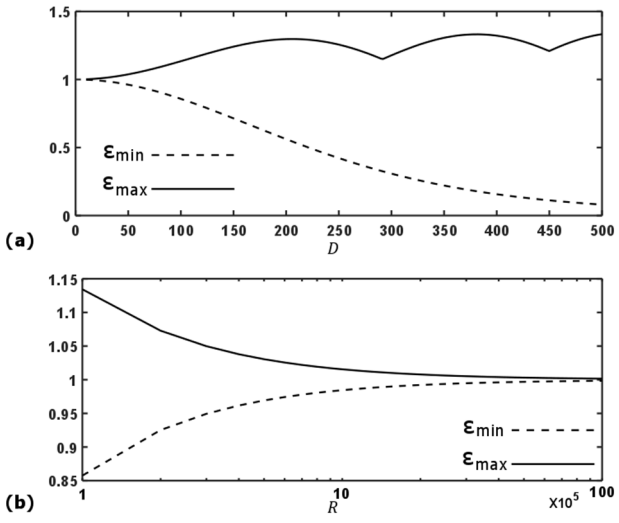

FIGURE 14. The minimum and maximum FSSR on an observation plane for a circular target. (a) The diameter of the circle is from 10 to 500 while distance R is fixed at 10^5. (b) Distance R is from 10^5 to 10^7 while the diameter of the circle is 100.

for any 3D shapes only the shadow silhouette plays a part in the FSSR, in our analysis we assume that all targets are only 2D and located on a plane parallel to the observation plane. The observation plane is assumed to be located at $R = 10^5$.

The true values of the FSSR is calculated with (5) and only samples on the line of $x = 0$ are used. From our previous analysis, it is suggested that the minimum FSSR can provide an estimate of the area of the target shadow profile. So in the first step of the retrieval, we find the minimum

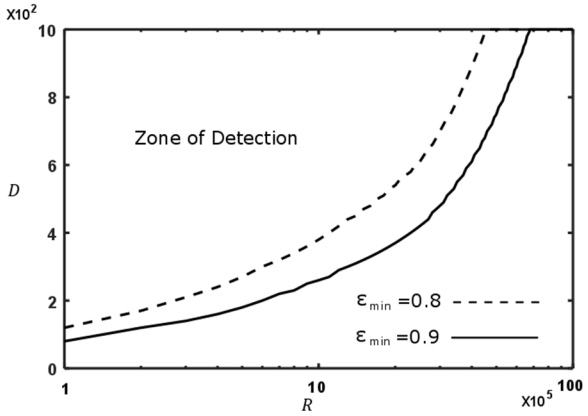

FIGURE 15. The R-D relationship when the minimum FSSR is 0.8 (dashed line) and 0.9 (solid line).

value of the FSSR samples and estimate the target shadow dimension using Fig. 14(a). This dimension will determine the number of strips needed and their width for the shadow profile retrieval.

The first numerical analysis was carried out using a triangular target, the dimensions of which is shown in Fig. 16(a). It can be considered a far-field scenario as the far-field parameter S is 0.8. The true values of the FSSR at different locations on the line of $x = 0$ on the observation plane are shown by the black curve in Fig. 16(b). Then we use a finite number of observations of ε to retrieve the approximate shadow profile of the target. In this case, 45 observation points (shown by the red circles in Fig. 16(b)) with a fixed increment in z are selected. Firstly, we estimate the size of the target by finding the minimum value of the observed ε (0.844 in Fig. 16(b)) and assuming that the target is circular shape. It is estimated that the observed the value of $\varepsilon_{\min}$ corresponds to a circle with diameter 105 (Fig. 14(a)). Based on the assumption that the target profile should have similar dimensions, for retrieval we allow a total width of 400, which approximately quadruples the estimated diameter of 105. Consequently, 20 strips each of which has a width of 20 are used to represent the shadow profile.

A nonlinear least-square function ('lsqnonlin' in MATLAB) with the trust-region-reflective algorithm is employed to find the optimal solution for strip heights h_p. Then the retrieved shadow profile is plotted on the $z' - x'$ plane (Fig. 17(b)). In Fig. 17(a), the approximated triangle using 20 strips (10 of which have a height of 0) is shown for comparison. It can be seen that the retrieved shadow profile agrees with the approximated triangle. We also plot the errors r_q and r'_q $(q = 1, \ldots, 45)$ in Fig. 16(c), where

$$r_q = \varepsilon_q(z_q) - \left| 1 - \frac{1}{iR} \sum_{p=1}^{20} h_p G_p(z_q) \right|^2, \qquad (34)$$

in which ε_q is the observed FSSR, h_p is the heights of strips in the approximated triangle (Fig. 17(a)). r'_q is computed

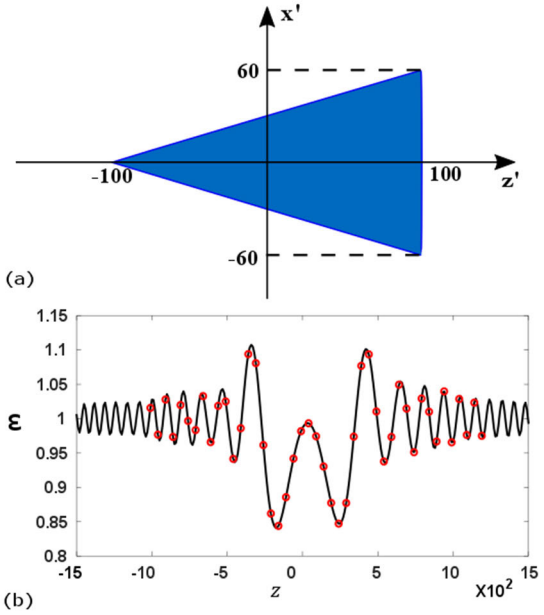

FIGURE 16. (a) Dimensions of the triangular target. (b) The true FSSR is shown by the black curve, and the observed FSSRs at 45 different locations are marked by the red circles.

using (34) by replacing h_p with h'_p, which is the retrieved heights (shown in Fig. 17(b)). Error r_q shows how much the approximation in (8) and (11) deviates from the true FSSR generated by the exact triangle and the Fresnel diffraction formula. Error r'_q shows the same deviation for the retrieved shadow profile. It can be seen that the error for the approximated triangle is in the order of 10^{-3} for all 45 observation points. The retrieved shadow profile in Fig. 17(b) generates very similar error to that of the approximated triangle.

A more complex shape is also used to examine the retrieval performance. The dimensions of the irregular shape is shown in Fig. 18(a) (the far-field parameter is the same as before), and the true FSSR generated by Fresnel diffraction is shown by the black curve in Fig. 18(b). There are 50 observation points which are shown by the red circles in Fig. 18(b). Note that the middle section of the target is not symmetric about the z-axis. Nonetheless, the retrieval algorithm can only obtain the heights of the strips so it is reasonable to place the midpoints of all the strips on the z'-axis.

Figure 19(a) shows the approximated shadow profile using 30 centered strips (12 of which have a height of 0) with width of 10. The retrieved shadow profile using 30 strips is shown in Fig. 19(b), which also displays good agreement with the approximated shadow profile. Errors r_q and $r_q{}'$ are shown in Fig. 19(c), both of which are in the order of 10^{-2} for the 50 observation points. The error due to the target's non-centerd middle section is not significant, which is as expected according the analysis in Section IV. The distance from the the z'-axis to the center of the middle section generally satisfies (22) for $R = 10^5$ and $h_p \approx 75$.

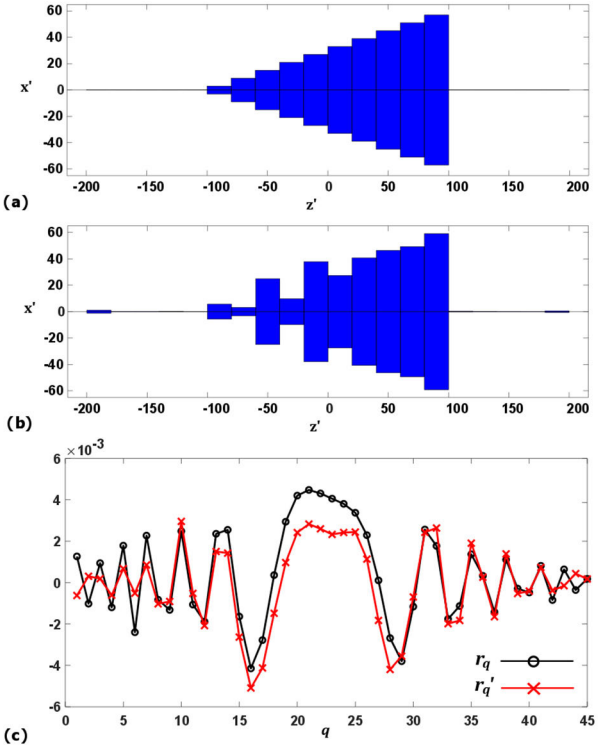

FIGURE 17. (a) The approximated shape where the original triangle is represented by 10 rectangular strips. (b) The retrieved shadow profile using the observed FSSRs at 45 locations. (c) The black circles show the error defined by (34) for the approximated triangle (a), and red crosses show the error for the retrieved shadow profile at 45 different locations.

C. ERROR DUE TO UNCENTERED LINE OF OBSERVATION AND SHADOW PROFILE DISCRETIZATION

We first investigate the impact of $x \neq 0$. For the triangular target in Fig. 16(a), with all the observation points moved to the line of $x = 80$ and all other parameters kept the same, the retrieved shape is shown in Fig. 20(a) and errors r_q and r_q' are shown in Fig. 20(b), in which it can be seen that the accuracy of the retrieval drops. When the observation points are moved further to the line of $x = 160$, the retrieval results are shown in Fig. 20(c) and (d). In this case the triangular shape is not visible anymore, suggesting that the error is too big for the retrieval. This is in line with our analysis in Section IV, which suggests that the desired resolution of 20 is not achievable if x is larger than 120.

For the shadow profile discretization, we reduce the resolution to 50 so there are only 4 strips of width 50 to approximate the triangle (Fig. 21(a)). The retrieved shape is shown in Fig. 21(b). Errors r_q and r_q' are also calculated and shown in Fig. 21(c). It can be seen that the errors are slightly higher than those produced by resolution of 20. This confirms that a lower resolution (wider strips) leads to a higher level of errors.

D. SHADOW PROFILE RETRIEVAL WITH NONLINEAR APPROXIMATION

Consider the triangular object in Fig. 16(a), if we use (32) instead of (30) in the nonlinear least-squares algorithm, i.e., include the cubic term of the Maclaurin series, the retrieved shadow profile is shown in Fig. 22(a). Errors r_q and r_q' are also

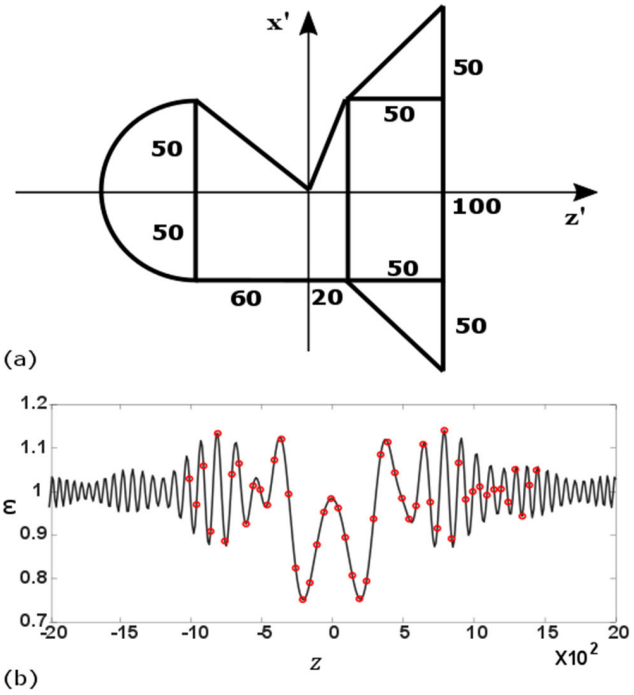

FIGURE 18. (a) The irregular shape. (b) The true FSSR is shown by the black curve, and the observed FSSRs at 50 different locations are marked by the red circles.

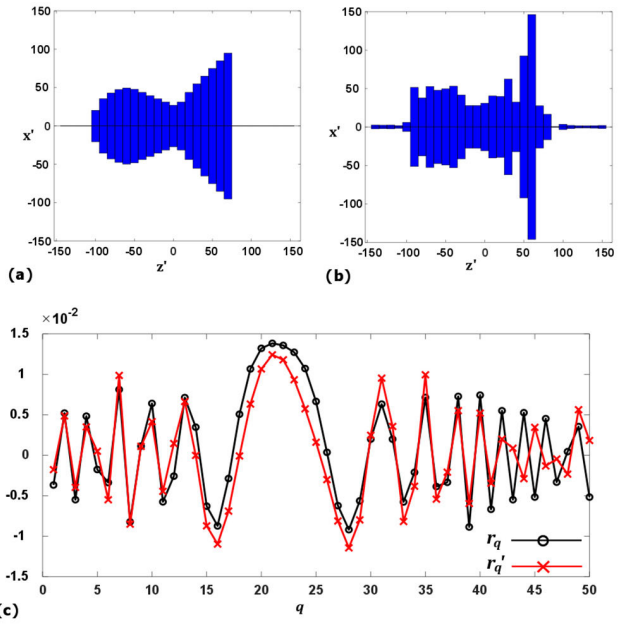

FIGURE 19. (a) The approximated shadow profile where the original irregular shape is replaced by 18 centered strips. (b) The retrieved shadow profile using the observed FSSRs at 50 locations. (c) The black circles show the error defined by (34) for the approximated shadow profile, and red crosses show the error for the retrieved shadow profile at 50 different locations.

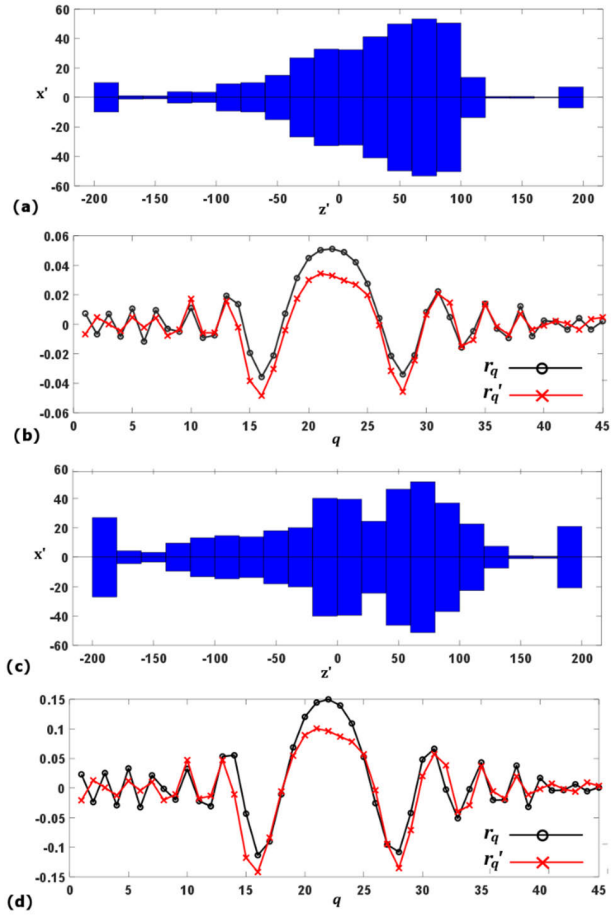

FIGURE 20. (a) The retrieved shape when the observation points are moved to the line of $x = 80$. (b) The errors define by (34) for $x = 80$. (c) The retrieved shape when the observation points are moved to the line of $x = 160$. (d) The errors define by (34) for $x = 160$.

calculated (shown in Fig. 22(b)) using the following updated equations:

$$r_q = \varepsilon_q(z_q) - \left| 1 - \frac{1}{iR} \sum_{p=1}^{20} h_p (1 + \frac{\pi}{12} \frac{h_p^2}{R\lambda} i) G_p\left(z_q\right) \right|^2, \quad (35)$$

where h_p is the approximated heights of the strips, r_q' is computed using (35) by replacing h_p with h'_p, which is the retrieved heights of the strips. It can be seen that including the cubic term has reduce the retrieval errors form the order of 10^{-3} (Fig. 17(c)) to the order of 10^{-4}.

If the dimensions of the triangular target are increased by 20% (length is 240 and height is 144), the far-field parameter is 1.152 so it is considered a close to near-field scenario. The retrieved shape using only the linear term of the Maclaurin series is shown in Fig. 23(a), and the result with the cubic term included is shown in Fig. 23(b). It can be seen that the retrieval accuracy is significantly improved when the cubic term is included.

The retrieval process including the cubic term has also been done for the complex shape in Fig. 18(a). Note that this shape

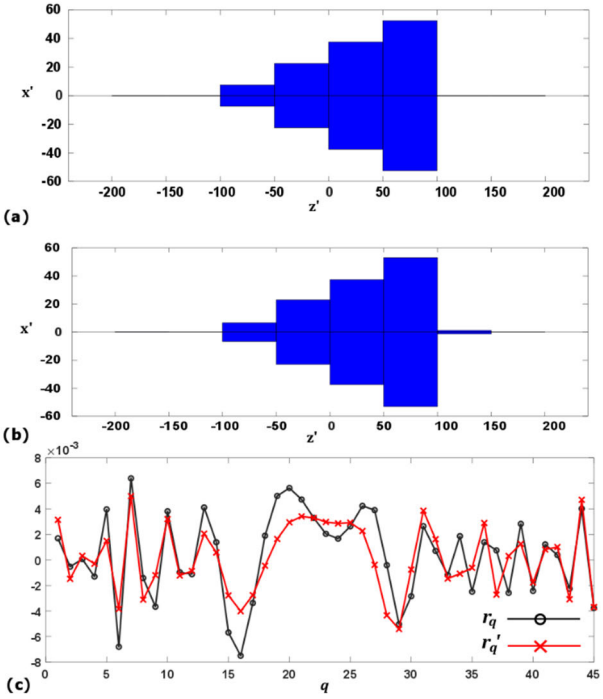

FIGURE 21. (a) The approximated shape where the original triangle is replaced by 4 rectangular strips. (b) The retrieved shape using the observed FSSRs at 45 locations. (c) The black circles show the error defined by (34) for the approximated shadow profile, and red crosses show the error for the retrieved shadow profile at 45 different locations.

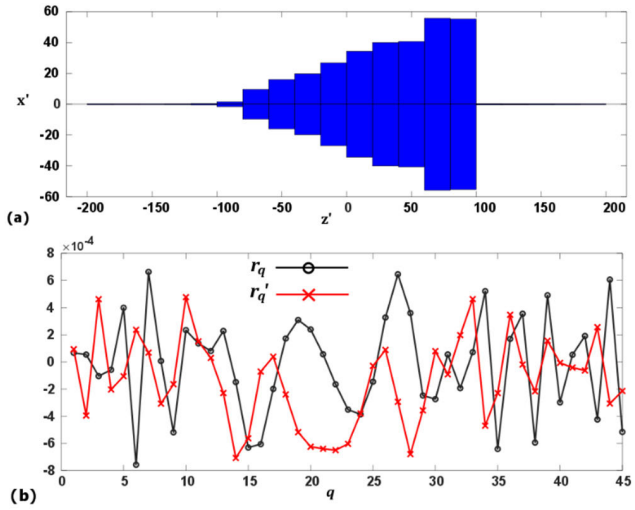

FIGURE 22. (a) The retrieved shadow profile for the triangular target with the cubic term included in the nonlinear least-squares. (b) The errors of the approximated shadow profile (black) and the retrieved shadow profile (red) at 45 different locations using (35).

is close to symmetric, so the approximation in (32) can be applied without introduction too big an error. The retrieved shadow profile is shown in Fig. 24(a) and the errors are shown in Fig. 24(b). Compared with Fig. 19, it can be concluded that

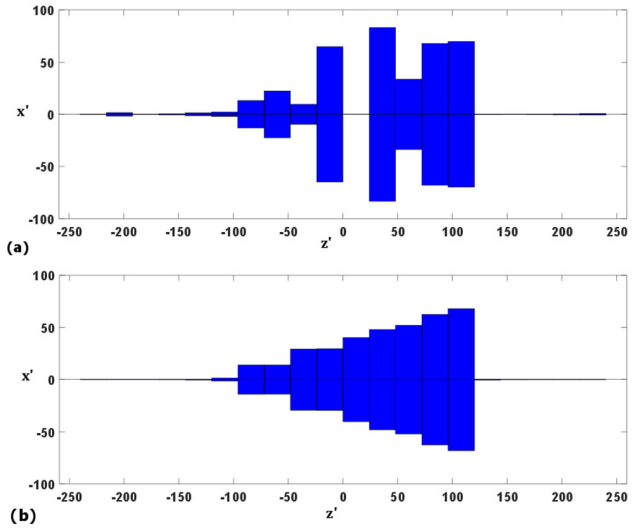

FIGURE 23. (a) The retrieved shadow profile for the triangular target in the close to near-field case with only the linear term included. (b) The retrieved shadow profile for the triangular target in the close to near-field case with both the linear and the cubic terms included.

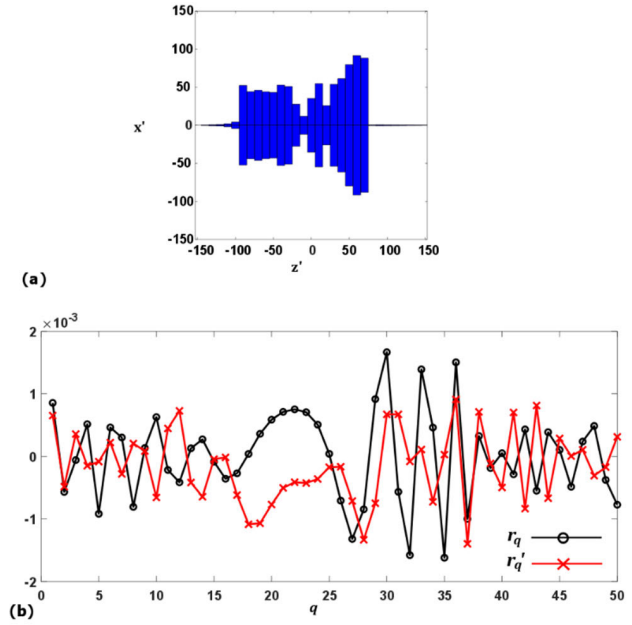

FIGURE 24. (a) The retrieved shadow profile for the irregular target with the cubic term included in the nonlinear least-squares. (b) The errors of the approximated shadow profile (black) and the retrieved shadow profile (red) at 50 different locations using (35).

the retrieval outcome is improved and the errors are less when the cubic term is taken into account.

E. ESTIMATION OF FSSR FROM THE TOTAL POWER FOR SHADOW PROFILE RETRIEVAL

In this section, we investigate shadow profile retrieval with the FSSR estimated through P_{tot}. From Fig. 13, we can see that as z moves further away from the origin, the difference

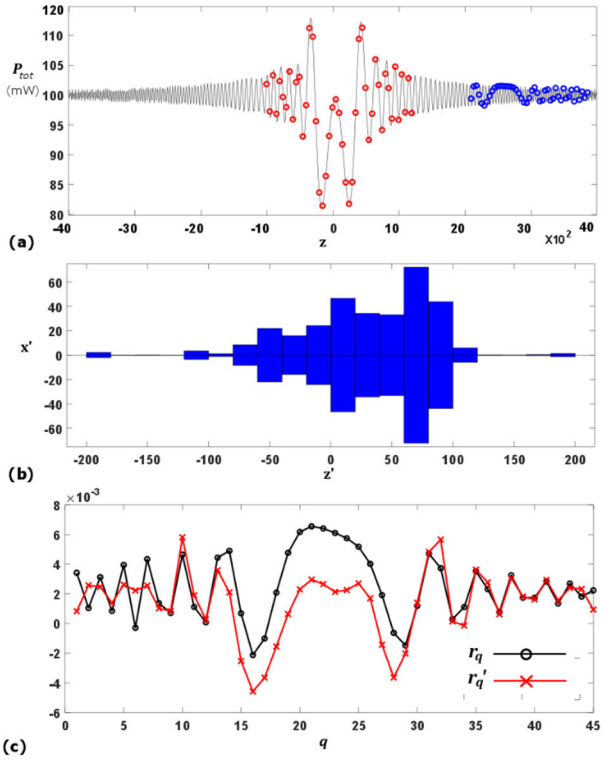

FIGURE 25. (a) The total received power for the triangular target in Fig. 15(a). The 45 samples used to estimate the total power are shown by the blue circles and the other 45 sample used for the retrieval are shown by the red circles. (b) The retrieved shadow profile. (c) The errors of the approximated shadow profile (black) and the retrieved shadow profile (red).

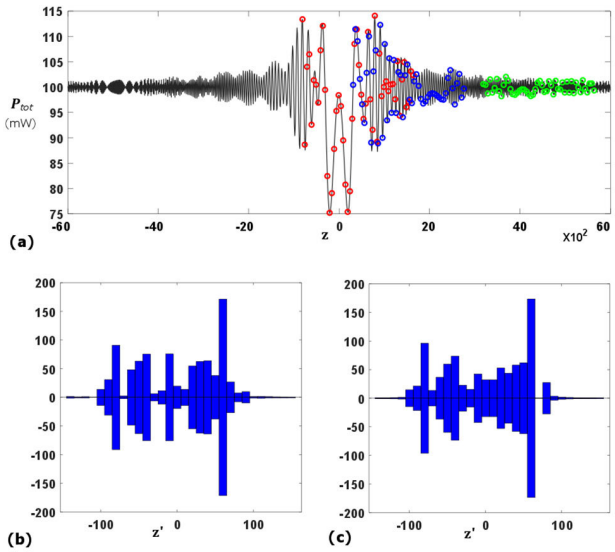

FIGURE 26. (a) The total received power for the irregular target in Fig. 17(a). The 50 samples used for the retrieval are shown by the red circles, blue and green circles represent the samples to calculate the DPS power for case one and two, respectively. (b) The retrieved shadow profile for case one. (c) The retrieved shadow profile for case two.

between P_{tot} and P_{inc} generally becomes less. If we take multiple samples of P_{tot} far away enough from the origin,

the average of these samples, denoted by P_{sam}, will be very close to P_{inc}. We apply this principle and try to retrieve the shadow profile for the triangular target in Fig. 16(a). We assume that P_{inc} is 100 mW and that P_{tot} (shown by the black line in Fig. 25(a)) is available for sampling on the line of $x = 0$ on the observation plane. For the estimation of P_{inc}, 45 samples of P_{tot} (shown by the blue circles in Fig. 25(a)) with a fixed increment in z are selected and then averaged. Secondly, another 45 samples of P_{tot} (shown by the red circles in Fig. 25(a)) are used to calculated the 45 observations of ε for the purpose of target profile retrieval. After that, the retrieval process is the same as that described in Section V-B. The retrieved shadow profile is shown in Fig. 25(b), which agrees with the true shape. The errors are plotted in Fig. 25(c), which are slightly higher than those in Fig. 17(c). This is due to the presence of estimation error in the FSSR.

The irregular target is also investigated using the same approach. In Fig. 26(a), P_{tot} is plotted by the black line while the 50 samples used to calculate ε for shadow profile retrieval are shown by the red circles. For case one we use 50 samples closer to the origin (shown by the blue circles in Fig. 26(a)) to estimate P_{inc} and the retrieved shadow profile is shown in Fig. 26(b). For case two we use 50 samples further away from the origin (shown by the green circles in Fig. 26(a)) to estimate P_{inc} and the retrieved shadow profile is shown in Fig. 26(c). It can be seen that the second retrieval result is slightly better due to less error in the estimated P_{inc}.

VI. CONCLUSION

In this paper, we introduce the concept of the FSSR of a target in a FSR system as the ratio of the total received power density to the incident power density for a receiver at a certain location. The FSSR shows directly how far the total received signal deviates from the DPS, which the FSCS does not provide. It is a more suitable parameter to describe the target in FSR systems.

Numerical results are used to demonstrate how the FSSR is affected by the normalized size and shape of the target and the location of the receiver. Using a circular target, we demonstrate that the minimum FSSR on an observation plane is a monotonically decreasing function of the normalized diameter, while the maximum FSSR is a non-monotonic function. When the distance of the observation plane from the target is increased, both the minimum and the maximum FSSR converge asymptotically to one.

Our mathematical analysis shows that the shadow profile of the target can be retrieved using a nonlinear least-square algorithm with the discrete observations of the FSSR. A triangular shape and an irregular shape are used to investigate the performance of the shadow profile retrieval. Our numerical results indicate that the retrieved shadow profiles represented by a finite number of rectangular strips display agreement with the original shapes. There are three sources of errors in the proposed retrieval algorithm. The first is due to the uncentered line of observation. The error in the retrieved heights becomes more significant as the line of observation deviates farther from the center. We demonstrate that the distance of the line of observation from the center can provide a reference as to if the desired resolution can be achieved. The second is due to approximating the original shadow profile with rectangular strips. The third is caused by the approximation of the imaginary error function using its Maclaurin series. Essentially, the far-field parameter determines the level of error induced by the approximation. Numerical results confirm that the error can be reduced by including the cubic term of the Maclaurin series in the retrieval algorithm. It is also suggested that the FSSR for shadow profile retrieval can be measured through the samples of the total received power, and that the power of the DPS is estimated more accurately when samples of the total power are taken where the magnitude of oscillation in the samples is relatively small.

Our investigations on the FSSR indicate that it can be useful in the analytical studies of FSR systems. As a parameter, the FSSR is relevant to target detection, classification, size estimation, and shadow profile imaging. In the future, we will investigate the effects of noise on our approach and design physical experiments.

REFERENCES

[1] Y. Blanchard, "A French pre-WW II attempt at air-warning radar: Pierre David's 'electromagnetic barrier,'" *URSI Radio Sci. Bull.*, vol. 2016, no. 358, pp. 18–34, Sep. 2016.

[2] H. Griffiths, "Early history of bistatic radar," in *Proc. Eur. Radar Conf. (EuRAD)*, Oct. 2016, pp. 253–257.

[3] V. Koch and R. Westphal, "New approach to a multistatic passive radar sensor for air/space defense," *IEEE Aerosp. Electron. Syst. Mag.*, vol. 10, no. 11, pp. 24–32, Nov. 1995, doi: 10.1109/62.473409.

[4] I. Suberviola, I. Mayordomo, and J. Mendizabal, "Experimental results of air target detection with a GPS forward-scattering radar," *IEEE Geosci. Remote Sens. Lett.*, vol. 9, no. 1, pp. 47–51, Jan. 2012, doi: 10.1109/LGRS.2011.2159477.

[5] I. Garvanov, C. Kabakchiev, V. Behar, and P. Daskalov, "Air target detection with a GPS forward-scattering radar," in *Proc. 19th Int. Symp. Electr. App. Technol. (SIELA)*, May 2016, pp. 1–4, doi: 10.1109/SIELA.2016.7543000.

[6] C. Clemente, T. Parry, G. Galston, P. Hammond, C. Berry, C. Ilioudis, D. Gaglione, and J. J. Soraghan, "GNSS based passive bistatic radar for micro-Doppler based classification of helicopters: Experimental validation," in *Proc. IEEE Radar Conf. (RadarCon)*, May 2015, pp. 1104–1108, doi: 10.1109/RADAR.2015.7131159.

[7] C. Kabakchiev, V. Behar, I. Garvanov, D. Kabakchieva, and H. Rohling, "Detection, parametric imaging and classification of very small marine targets emerged in heavy sea clutter utilizing GPS-based forward scattering radar," in *Proc. IEEE Int. Conf. Acoust., Speech Signal Process. (ICASSP)*, May 2014, pp. 793–797, doi: 10.1109/ICASSP.2014.6853705.

[8] Chr. Kabakchiev, I. Garvanov, V. Behar, D. Kabakchieva, K. Kabakchiev, H. Rohling, K. Kulpa, and A. Yarovoy, "Detection and classification of objects from their radio shadows of GPS signals," in *Proc. 16th Int. Radar Symp. (IRS)*, Jun. 2015, pp. 906–911, doi: 10.1109/IRS.2015.7226336.

[9] M. Contu, A. De Luca, S. Hristov, L. Daniel, A. Stove, M. Gashinova, M. Cherniakov, D. Pastina, P. Lombardo, A. Baruzzi, and D. Cristallini, "Passive multifrequency forward-scatter radar measurements of airborne targets using broadcasting signals," *IEEE Trans. Aerosp. Electron. Syst.*, vol. 53, no. 3, pp. 1067–1087, Jun. 2017, doi: 10.1109/TAES.2017.2649198.

[10] M. Di Seglio and F. Colone, "DVB-T based forward scatter radar for small target surveillance," in *Proc. IEEE Radar Conf.*, Sep. 2020, pp. 1–6, doi: 10.1109/RadarConf2043947.2020.9266416.

[11] R. S. A. R. Abdullah, S. A. Musa, N. E. A. Rashid, A. Sali, A. A. Salah, and A. Ismail, "Passive forward-scattering radar using digital video broadcasting satellite signal for drone detection," *Remote Sens.*, vol. 12, no. 18, p. 3075, Sep. 2020.

[12] F. Colone, T. Martelli, and P. Lombardo, "Quasi-monostatic versus near forward scatter geometry in WiFi-based passive radar sensors," *IEEE Sensors J.*, vol. 17, no. 15, pp. 4757–4772, Aug. 2017, doi: 10.1109/JSEN.2017.2713450.
[13] T. Martelli, F. Colone, and P. Lombardo, "First experimental results for a WiFi-based passive forward scatter radar," in *Proc. IEEE Radar Conf. (RadarConf)*, May 2016, pp. 1–6, doi: 10.1109/RADAR.2016.7485108.
[14] A. Losito, M. Stentella, T. Martelli, and F. Colone, "Automatic vehicles classification approaches for WiFi-based passive forward scatter radar," in *Proc. Int. Conf. Radar Syst. (Radar)*, Oct. 2017, pp. 1–6, doi: 10.1049/cp.2017.0401.
[15] P. Krysik, K. Kulpa, and P. Samczynski, "GSM based passive receiver using forward scatter radar geometry," in *Proc. 14th Int. Radar Symp. (IRS)*, vol. 2, Jun. 2013, pp. 637–642.
[16] V. V. Chapurskiy and V. N. Sablin, "SISAR: Shadow inverse synthetic aperture radiolocation," in *Proc. Rec. IEEE Int. Radar Conf.*, May 2000, pp. 322–328, doi: 10.1109/RADAR.2000.851854.
[17] C. Hu, C. Liu, R. Wang, L. Chen, and L. Wang, "Detection and SISAR imaging of aircrafts using GNSS forward scatter radar: Signal modeling and experimental validation," *IEEE Trans. Aerosp. Electron. Syst.*, vol. 53, no. 4, pp. 2077–2093, Aug. 2017, doi: 10.1109/TAES.2017.2683578.
[18] C. Hu, L. Wang, and C. Liu, "SISAR imaging method based on GNSS signal: Theory and experimental results," in *Proc. CIE Int. Conf. Radar (RADAR)*, Oct. 2016, pp. 1–5, doi: 10.1109/RADAR.2016.8059223.
[19] D. Olivadese, E. Giusti, D. Petri, M. Martorella, A. Capria, and F. Berizzi, "Passive ISAR with DVB-T signals," *IEEE Trans. Geosci. Remote Sens.*, vol. 51, no. 8, pp. 4508–4517, Aug. 2013, doi: 10.1109/TGRS.2012.2236339.
[20] S. Cakaj, "The parameters comparison of the '*Starlink*' LEO satellites constellation for different orbital shells," *Frontiers Commun. Netw.*, vol. 2, May 2021, Art. no. 643095, doi: 10.3389/frcmn.2021.643095.
[21] X. Shen, D. D. Huang, B. Song, C. Vincent, and R. Togneri, "3-D tomographic reconstruction of rain field using microwave signals from LEO satellites: Principle and simulation results," *IEEE Trans. Geosci. Remote Sens.*, vol. 57, no. 8, pp. 5434–5446, Aug. 2019, doi: 10.1109/TGRS.2019.2899391.
[22] K. Song, X. Liu, T. Gao, and B. He, "Raindrop size distribution retrieval using joint dual-frequency and dual-polarization microwave links," *Adv. Meteorol.*, vol. 2019, Jun. 2019, Art. no. 7251870, doi: 10.1155/2019/7251870.
[23] X. Shen, D. D. Huang, W. Wang, A. F. Prein, and R. Togneri, "Retrieval of cloud liquid water using microwave signals from LEO satellites: A feasibility study through simulations," *Atmosphere*, vol. 11, no. 5, p. 460, May 2020. [Online]. Available: https://www.mdpi.com/2073-4433/11/5/460
[24] D. D. Huang, "Passive positioning of flying object with microwave signals from LEO satellites: Concept and preliminary simulation results," *IEEE Access*, vol. 9, pp. 14640–14648, 2021, doi: 10.1109/ACCESS.2021.3052535.
[25] I. Theodorou, C. V. Ilioudis, C. Clemente, and M. Vasile, "SISAR imaging–radio holography signal reconstruction based on receiver-transmitter motion," in *Proc. IEEE Radar Conf. (RadarConf)*, Apr. 2019, pp. 1–6, doi: 10.1109/RADAR.2019.8835596.
[26] I. Theodorou, C. Ilioudis, C. Clemente, M. Vasile, and J. Soraghan, "SISAR imaging for space debris based on nanosatellites," *IET Radar, Sonar Navigat.*, vol. 14, no. 8, pp. 1192–1201, Aug. 2020, doi: 10.1049/iet-rsn.2019.0574.
[27] L. Creed, J. Graham, C. Jenkins, S. D. Riofrio, A. Wilson, and M. Vasile, "STRATHcube: The design of a CubeSat for space debris detection using in-orbit passive bistatic radar," in *Proc. 72nd Int. Astron. Congr.*, 2021, pp. 1–13.
[28] D. Huang, "Doppler analysis of forward scattering radar with opportunistic signals from LEO satellites," *IEEE Access*, vol. 10, pp. 109597–109608, 2022, doi: 10.1109/ACCESS.2022.3214844.
[29] J. Glaser, "Bistatic RCS of complex objects near forward scatter," *IEEE Trans. Aerosp. Electron. Syst.*, vol. AES-21, no. 1, pp. 70–78, Jan. 1985, doi: 10.1109/TAES.1985.310540.
[30] A. B. Blyakhman and I. A. Runova, "Forward scattering radiolocation bistatic RCS and target detection," in *Proc. IEEE Radar Conf., Radar Next Millennium*, Apr. 1999, pp. 203–208, doi: 10.1109/NRC.1999.767314.
[31] C. Hu, C. Zhou, T. Zeng, and T. Long, "Radio holography signal reconstruction and shadow inverse synthetic aperture radar imaging in ground-based forward scatter radar: Theory and experimental results," *IET Radar, Sonar Navigat.*, vol. 8, no. 8, pp. 907–916, Oct. 2014, doi: 10.1049/iet-rsn.2013.0267.
[32] N. Ustalli, P. Lombardo, and D. Pastina, "Detection performance of a forward scatter radar using a crystal video detector," *IEEE Trans. Aerosp. Electron. Syst.*, vol. 54, no. 3, pp. 1093–1114, Jun. 2018, doi: 10.1109/TAES.2017.2774659.
[33] J. W. Goodman, *Introduction to Fourier Optics*. New York, NY, USA: McGraw-Hill, 1996.
[34] T. F. Coleman and Y. Li, "An interior trust region approach for nonlinear minimization subject to bounds," *SIAM J. Optim.*, vol. 6, no. 2, pp. 418–445, May 1996, doi: 10.1137/0806023.
[35] M. Gashinova, L. Daniel, V. Sizov, E. Hoare, and M. Cherniakov, "Phenomenology of Doppler forward scatter radar for surface targets observation," *IET Radar, Sonar Navigat.*, vol. 7, no. 4, pp. 422–432, Apr. 2013, doi: 10.1049/iet-rsn.2012.0233.
[36] M. Falconi, D. Comite, A. Galli, D. Pastina, P. Lombardo, and F. Marzano, "Forward scatter radar for air surveillance: Characterizing the target-receiver transition from far-field to near-field regions," *Remote Sens.*, vol. 9, no. 1, p. 50, Jan. 2017.
[37] M. Gashinova, L. Daniel, A. Myakinkov, and M. Cherniakov, *Novel Radar Techniques and Applications Volume 1: Real Aperture Array Radar, Imaging Radar, and Passive and Multistatic Radar*. Rijeka, Croatia: SciTech, 2017.
[38] E. Wolf and E. W. Marchand, "Comparison of the Kirchhoff and the Rayleigh–Sommerfeld theories of diffraction at an aperture," *J. Opt. Soc. Amer.*, vol. 54, no. 5, pp. 587–594, May 1964, doi: 10.1364/JOSA.54.000587.
[39] M. T. Falconi, P. Lombardo, D. Pastina, and F. S. Marzano, "A closed-form model for long- and short-range forward scatter radar signals from rectangular conductive targets," *IEEE Trans. Aerosp. Electron. Syst.*, vol. 56, no. 2, pp. 1370–1390, Apr. 2020, doi: 10.1109/TAES.2019.2933974.
[40] L. C. Andrews, *Special Functions of Mathematics for Engineers*, 2nd ed. Oxford, U.K.: Oxford Univ. Press, 1997.

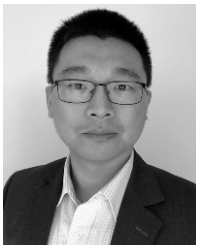

XI SHEN (Member, IEEE) received the B.E.E.E. degree in electronic engineering from Tsinghua University, Beijing, China, in 2003, and the Ph.D. degree in electronic engineering from the Imperial College London, London, U.K., in 2006.

He was with China Unicom as a Telecommunication Engineer and then a Senior Engineer for eight years. He is currently a Research Associate with the School of Electrical, Electronic, and Computer Engineering, The University of Western Australia, Perth, Australia. His research interests include environmental monitoring using microwave communication links, signal processing in satellite communication, and forward scatter radar.

DEFENG (DAVID) HUANG (Senior Member, IEEE) received the B.E.E.E. and M.E.E.E. degrees in electronic engineering from Tsinghua University, Beijing, China, in 1996 and 1999, respectively, and the Ph.D. degree in electrical and electronic engineering from The Hong Kong University of Science and Technology (HKUST), Hong Kong, in 2004.

Before joining The University of Western Australia (UWA), he was a Lecturer with Tsinghua University. In 2005, he joined the School of Electrical, Electronic and Computer Engineering, UWA, as a Lecturer, where has been promoted to be a Professor, since 2011. He served as an Editor for the IEEE TRANSACTIONS ON WIRELESS COMMUNICATIONS and the IEEE WIRELESS COMMUNICATIONS LETTERS, from 2005 to 2011 and from 2011 to 2015, respectively, and an Editorial Assistant for the IEEE TRANSACTIONS ON WIRELESS COMMUNICATIONS, from 2002 to 2004.